Flexible Solid-State Asymmetric Supercapacitors with Enhanced Performance Enabled by Free-Standing MXene—Biopolymer Nanocomposites and Hierarchical Graphene—RuO$_x$ Paper Electrodes

Leiqiang Qin,*[a] Quanzheng Tao,[a] Lianlian Liu,[a] Jianxia Jiang,[a, d] Xianjie Liu,[b] Mats Fahlman,[b, c] Lintao Hou,[d] Johanna Rosen,*[a] and Fengling Zhang*[a, d]

Two-dimensional (2D) transition metal carbides and carbonitrides, called MXenes, with metallic conductivity and hydrophilic surfaces, show great promise as electrode materials for supercapacitors. A major drawback of 2D nanomaterials is the re-stacking of the nanosheets, which prevents full utilization of surface area and blocks the access of the electrolyte. In this study, a free-standing nanocomposite paper electrode is realized by combining Mo$_{1.33}$C MXene and positively charged biopolymer lignin (the second most abundant biopolymer in nature, L-DEA). The self-assembled layered architecture with alternating polymer and MXene flakes increases the interlayer space to promote ion transport, and with combining charge storage capability of the lignin derivative and MXene in an interpenetrating MXene/L-DEA nanocomposite, which offers an impressive capacitance of 503.7 F g^{-1}. Moreover, we demonstrate flexible solid-state asymmetric supercapacitors (ASCs) using Mo$_{1.33}$C@L-DEA as the negative electrode and electrochemically exfoliated graphene with ruthenium oxide (EG@RuO$_x$) as the positive electrode. This asymmetric device operates at a voltage window of 1.35 V, which is about two times wider than that of a symmetric Mo$_{1.33}$C@L-DEA based supercapacitor. Finally, the ASCs can deliver an energy density of 51.9 Wh kg^{-1} at a power density of 338.5 W kg^{-1}, with 86% capacitance retention after 10000 charge-discharge cycles.

1. Introduction

With fast-growing demand for portable and clean energy sources, electrochemical capacitors have been attracting increased attention because of their much greater power density and cyclability than Li batteries.[1,2] To achieve rapid ion access to the available electrochemically active centers, various nanomaterials, such as nanoparticles (0D),[3] nanowires and nanotubes (1D),[4] layered materials (2D)[5] and mesoporous

structures (3D)[6] have been explored. 2D and layered materials that can be intercalated and exfoliated have shown great potential for high-performance energy storage devices. MXenes are a family of 2D transition metal carbides and nitrides, which combine good electrical conductivity due to the inner conductive carbide layers, and hydrophilic transition metal oxide surfaces.[7] MXenes are synthesized by extracting the "A" layers (typically Al) from the layered carbides or carbonitrides known as MAX phases.[8,9] The latter exhibit layered hexagonal structures with a general formula of M$_{n+1}$AX$_n$ ($n = 1$, 2, 3), where M represents a transition metal, A usually represents a III A or IV A element (like Al, Ga, Si, or Ge), and X represents either C or/and N.[10] Most recently, we reported a new type of MAX phase, *i*-MAX, realizing an in-plane vacancy ordering.[11,12] Apart from a high conductivity, the first vacancy Mo$_{1.33}$C MXene show a good potential for supercapacitor applications.[13,14]

The intercalation phenomenon is observed in many materials with layered structures, such as clay[15] and graphite,[16] which have rather weak bonding in-between layers. A similar concept applies to MXenes, through selectively remove of atomic layers to facilitate 2D materials. This delamination of the multilayered MXene materials into single- or few-layer nanosheets dramatically increases the accessible surfaces.[17–22] However, the re-stacking of layers during the preparation of the films significantly weakens the effect of the intercalation. Recently, a research has shown that an improved charge storage capacity of MXene based supercapacitor electrodes can be achieved by increasing the interlayer spacing of Ti$_3$C$_2$T$_x$ MXene, using the intercalation of a polymer (polyvinyl alcohol

[a] Dr. L. Qin, Q. Tao, L. Liu, Dr. J. Jiang, Prof. J. Rosen, Prof. F. Zhang
Department of Physics, Chemistry and Biology (IFM)
Linköping University,
SE-58183, Linköping, Sweden
E-mail: leiqiang.qin@liu.se
johanna.rosen@liu.se
fengling.zhang@liu.se

[b] Dr. X. Liu, Prof. M. Fahlman
Laboratory of Organic Electronics,
Department of Science and Technology
Linköping University,
SE-60174, Norrköping, Sweden

[c] Prof. M. Fahlman
Wallenberg Wood Science Center
Linköping University,
SE-60174, Norrköping, Sweden

[d] Dr. J. Jiang, Prof. L. Hou, Prof. F. Zhang
Guangzhou Key Laboratory of Vacuum Coating Technologies and New Energy Materials,
Physics Department
Jinan University,
510632, Guangzhou, PR China

(PVA) and charged polydiallyldimethylammonium chloride (PDDA)).[23] Capacitance is further improved when electrochemically active polymers are confined between the MXene layers, due to the redox behavior of polymers.[13,24–26] For further improvement of the material properties, it is necessary to gain a fundamental understanding of the interactions between the polymers and the MXene surfaces.

Electrochemically active biopolymers containing phenol and quinone compounds are widely present in plants. Lignin, a by-product from paper processing, contains a large number of phenol and quinone groups, which can store charges by reversible reduction-oxidation conversion.[27] It is mainly burnt to produce process heat or used as surfactant in the processing of cement. Indeed, lignin is a cheap and scalable material, however, the above uses only cover a small fraction of this low value product. Inganäs and Milczarek demonstrated the charge storage capability of lignin in combination with polypyrrole in an aqueous based electrolyte.[28] A conductive addictive herein is necessary to enable the charge transport as lignin is electronic insulating. Since then, various combinations of lignin and conductive materials such as carbon nanotubes,[29] reduced graphene oxide,[30] and conducting polymers[31,32] have been investigated as electrode materials for energy storage. However, the reports on MXene and biopolymer composites as electrode materials for supercapacitor applications are limited. In addition, ASCs are an effective design to increase cell voltage in aqueous electrolyte by coupling different positive and negative electrode materials with well-separated potential windows.[33,34] Herein, amine cations functionalized lignin (L-DEA) with positive charges is prepared by Mannich reaction, followed by intercalated with the negative charged $Mo_{1.33}C$ MXene through electrostatic self-assembly. The increased interlayer spacing of $Mo_{1.33}C$ nanosheets significantly facilitates the charge transport needed in electrodes for supercapacitors (Figure 1a). The $Mo_{1.33}C@L-DEA$ composite paper electrodes, obtained from solution processable $Mo_{1.33}C$ MXene and L-DEA hybrid ink, exhibit excellent capacitance, high rate performance and great cycling stability. Furthermore, ASCs are constructed based on the $Mo_{1.33}C@L-DEA$ and $EG@RuO_x$ composite paper electrodes, and achieve a high energy density of 51.9 Wh kg^{-1} and power density of 40095 W kg^{-1}, at 1.35 V.

2. Results and Discussion

The amine cations functionalized lignin is synthesized by Mannich reaction (see the experimental section for details). Vibrational spectra can provide the structural information on organic molecules, especially for functional group modified molecules. The FT-IR spectra of lignosulfonate and L-DEA are shown in Figure 1b. The lignin spectrum presents peaks at 1600 and 1505 cm^{-1} attributed to the vibrations of the aromatic rings, and bands at 1460 and 1422 cm^{-1} related to the aromatic ring vibrations combined with methyl and methylene C—H deformations. A broad peak is observed at 1215 cm^{-1} due to C—C and C—O stretching vibrations merged with aromatic ring stretching modes. These results are consistent with the
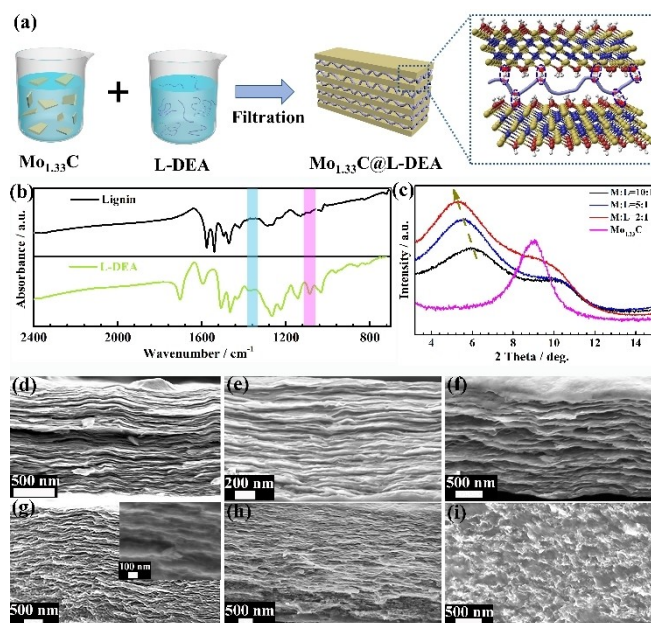

Figure 1. MXene/L-DEA nanocomposites. a) Schematic illustration of the preparation $Mo_{1.33}C@L-DEA$. b) FT-IR spectra of the lignin and L-DEA. c) XRD patterns of the hybrids and pristine $Mo_{1.33}C$ films. SEM cross-sectional images of d) $Mo_{1.33}C$ MXene, e) M:L=10:1, f) M:L=5:1, g) M:L=2:1, h) M:L=1:1, i) M:L=1:5.

previously reported lignin spectra.[35] For L-DEA, apart from the characteristic vibration spectrum of lignin, additional peaks are observed at 1373 cm^{-1} and 1087 cm^{-1} due to CH$_3$—N and C—N stretching vibrations, respectively. These FT-IR observations indicate that lignin has been successfully functionalized by amine cations. In addition, the zeta potential of lignin (−33.1 mV) changes from negative to positive (37.9 mV of L-DEA), which is consistent with the spectrum result (Figure S1, Supporting Information).

The synthetic strategy for the preparation of MXene@L-DEA composite paper electrodes containing different mass ratios of MXene and L-DEA are carried out. The composite paper electrodes are prepared by vacuum filtration of the mixture of the $Mo_{1.33}C$ colloidal solution and L-DEA solution. The X-ray diffraction (XRD) patterns of the pristine $Mo_{1.33}C$ film and the composite paper electrode are present in Figure 1c. The pristine MXene film shows a major peak at ~9°, which originates from the stacks of a few-layer $Mo_{1.33}C$ MXene sheets. For the composite paper electrodes, the peaks exhibit a clear gradual downshift from ~9° to ~5.3°, indicating an increase of ≈7 Å in the spacing between the $Mo_{1.33}C$ layers. This shift is attributed to polymer intercalating between $Mo_{1.33}C$ MXene nanosheets. However, the XRD peak almost disappears with the mass ratio of MXene and L-DEA being higher than 1:1 (Figure S3, Supporting Information). This indicates that the regular packing of the MXene nanosheets is hindered when the biopolymer content is high. The cross-sectional scanning electron microscopy (SEM) imaging (Figure 1d–i) of the $Mo_{1.33}C$ and the composite paper electrodes are recorded for studying the evolution of the morphology. The composite paper electrode of a 10:1 mass ratio exhibits well-aligned layered

Batteries & Supercaps

Articles
doi.org/10.1002/batt.202000044

Chemistry
Europe
European Chemical
Societies Publishing

morphology (Figure 1e), similar to the pristine $Mo_{1.33}C$ film (Figure 1d). With increasing the amount of intercalated L-DEA up to 2:1, the layered morphology of the composite paper electrode is still attained. The laminated structure is, however, less clear at mass ratios ($Mo_{1.33}C$:L-DEA) of 1:1 and 1:5. This corresponds to the results of XRD. The branched structure of the L-DEA chains and the intercalation between L-DEA and $Mo_{1.33}C$ increased the interlayer spacing and prevent the re-stacking of the $Mo_{1.33}C$ nanosheets.

The electrochemical performance of an electrode largely depends on the morphology and surface area of the electrode material. In order to evaluate the electrochemical properties of these composite paper electrodes with different M:L ratios, we conducted cyclic voltammetry (CV) experiments (Figure 2a) in 1 M H_2SO_4 at the scan rate of 50 mV/s, in the potential window from -0.35 to 0.3 V vs. Ag/AgCl. Compared with pristine $Mo_{1.33}C$, the composite paper electrodes exhibit more pronounced redox peaks between 0.1–0.2 V and -0.3–-0.2 V. This is attributed to the improved accessibility of the MXene surfaces and more efficient charge transfer caused by intercalation of the biopolymer chains. We also plot the capacitance of each sample in histograms in Figure S4, which clearly shows

that the $Mo_{1.33}C$@L-DEA composite yields the highest capacitance at a mass ratio of 2:1.

From this point forward, we focus on the samples with the best performance, i.e. with a 2:1 mass ratio of $Mo_{1.33}C$ to L-DEA. For the detailed study of the electrochemical performance of the composite paper electrodes, typical CV curves of the M:L=2:1 composite paper electrode at different scan rates are displayed in Figure 2b. The CV curves remain rectangular at the scan rate up to 1000 mVs^{-1}, which indicates a low resistance and fast ion transportation. Herein, the biopolymer chain enlarges the interlayer spacing between the MXene flakes, which facilitates efficient intra and inter-chain charge transport. It also potentially increases the accessibility to deep traps and facilitates ion transport. The nearly triangular galvanostatic charge/discharge (GCD) curves, see Figure 2c, of the M:L=2:1 composite film at different current densities confirm the high reversibility of the redox reactions and good coulomb efficiency ($\approx 93\%$), which is in good agreement with the CV curves. In addition, the rate performance of the M:L=2:1 composite paper electrode is presented in Figure 2d. At 1 Ag^{-1}, the composite film exhibits a high gravimetric capacitance of 503.7 Fg^{-1}, even at the current density of 30 Ag^{-1}, it yields a high capacitance of 405.9 Fg^{-1}. The high capacitance may be attributed to the redox contributions from both $Mo_{1.33}C$ and L-DEA, as well as the facile ionic transport channels provided by the aligned biopolymer network between the metallic MXene layers. The electrochemical capacitive behavior of the composite paper electrode is further investigated by electrochemical impedance spectroscopy (EIS), as shown in Figure 2e. At the low frequency of Nyquist plots, the slope is close to 90°, which indicates fast ion diffusion. In the high frequency region, the composite film shows a quite small charge-transport resistance with an almost invisible semicircle. Furthermore, the cyclic performance of the M:L=2:1 composite electrode is present in Figure 2f and it shows an 86% capacitance retention after 10000 cycles at a charging/discharging rate of 10 Ag^{-1}.

Based on above results, the $Mo_{1.33}C$@L-DEA composite paper electrodes feature high-rate performance, high specific gravimetric capacitances, and excellent cycling stability, however, limited operating voltage windows (~ 0.65 V). Since $Mo_{1.33}C$@L-DEA composite paper electrode as a pseudocapacitive material mainly operates at the negative potential window, it can construct an asymmetric supercapacitor with a positive pseudocapacitive material to obtain a wider potential window, which will result in a higher energy density than a symmetric structure (the energy density is proportional to the square of the potential window). Therefore, the graphene/RuO_x composite paper electrode by in situ growth of RuO_x on the surface of electrochemically exfoliated graphene (EG) through the sol-gel method (the details can be found in the experimental section) is fabricated. The EG is chosen in our study as the substrate for the direct deposition of RuO_x without the need of any surface pretreatment or use of binders or conductive additives. The free-standing EG@RuO_x composite films can be prepared by vacuum filtration. The cross-section SEM images of EG@RuO_x composite films and EG are shown in Figure 3a and Figure S7 (Supporting Information). The EG film exhibits a loose three-

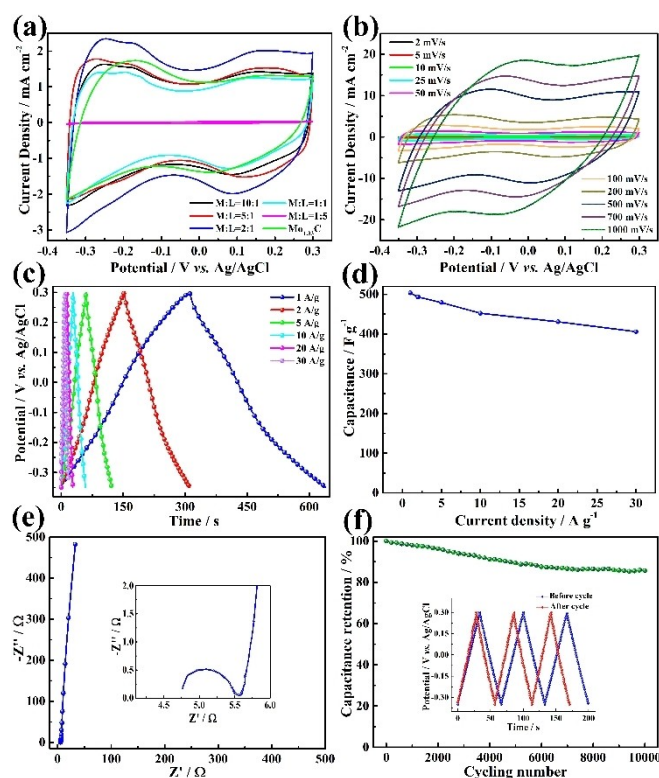**Figure 2.** Electrochemical performances of $Mo_{1.33}C$@L-DEA composite paper electrodes. (a) Comparison between cyclic voltammograms (CVs) of pristine $Mo_{1.33}C$ MXene and $Mo_{1.33}C$@L-DEA hybrid electrodes. b) CVs of M:L=2:1 composite paper electrode at scan rates from 2 mVs^{-1} to 1 Vs^{-1}. c) charge/discharge profiles of M:L=2:1 composite paper electrode at different current density. d) Gravimetric rate performances of M:L=2:1 composite paper electrode. e) Electrochemical impedance spectroscopy (EIS) data of the M:L=2:1 composite paper electrode. f) Cyclic stability of the $Mo_{1.33}C$@L-DEA electrode, inset: GCD data of the $Mo_{1.33}C$@L-DEA electrode before and after cycle.
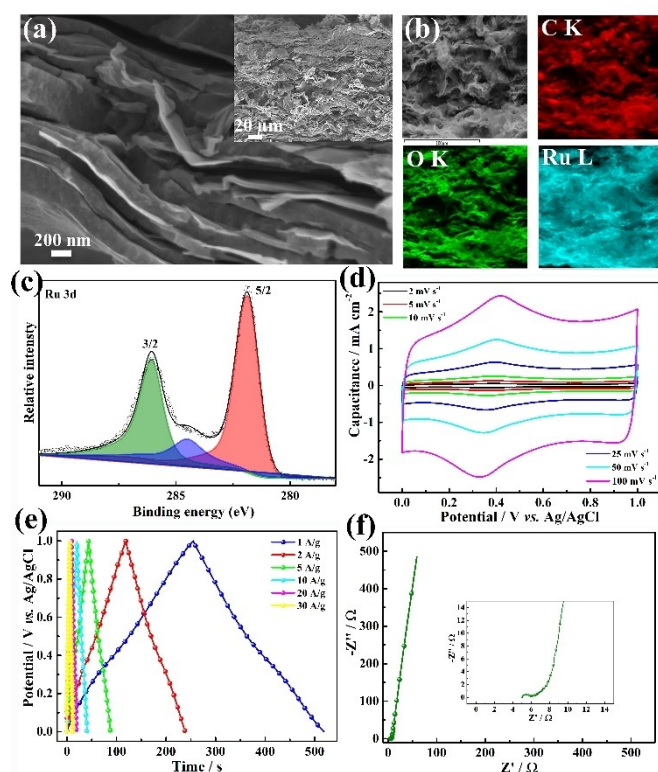
Figure 3. EG@RuO$_x$ composite paper electrode. a) Cross-sectional SEM image of EG@RuO$_x$ composite paper electrode, inset: Low-magnification cross-sectional SEM image of EG@RuO$_x$ composite paper electrode, b) EDS elemental mapping of cross-sectional EG@RuO$_x$ composite paper electrode, c) XPS result of the Ru 3d spectra, d) CVs of EG@RuO$_x$ composite paper electrode at scan rates from 2 mV s^{-1} to 100 mV s^{-1}, e) charge/discharge profiles of EG@RuO$_x$ hybrid electrode at different current density, f) electrochemical impedance spectroscopy (EIS) data of the EG@RuO$_x$ hybrid electrode.

dimensional microstructure consists of layered graphene. The EG@RuO$_x$ composite paper electrode displays a less clear layered stacking morphology at low magnification (Figure 3a inset). However, a higher magnification image of the composite paper electrode in Figure 3a reveals that the RuO$_x$ grows on the surface of EG and exhibits a structure of alternating EG and RuO$_x$. This structure not only prevents the aggregation of graphene but also makes full use of the surface area of graphene to promote electron transport between RuO$_x$ and graphene. In addition, energy dispersive X-ray spectroscopy (EDX) elemental mapping is used to study the element distribution of EG@RuO$_x$ (Figure 3b). EDX mapping of Ru confirms a homogeneous distribution of RuO$_x$ throughout the 3D composite frameworks. The X-ray photoelectron spectroscopy (XPS) data shown in Figure 3c confirms the incorporation of RuO$_x$ in the composite film by the sol-gel method.

The electrochemical performance of EG@RuO$_x$ composite paper electrode is performed in a three-electrode configuration in 1 M H$_2$SO$_4$. CVs of EG@RuO$_x$ clearly shows a pair of very broad redox peaks in the chosen potential window (0–1.0 V $vs.$ Ag/AgCl), which is indicative of the pseudocapacitive behavior of RuO$_x$ (Figure 3d). Besides, the shapes of the CV curves remain pseudo-rectangular, even at high scan rate, which indicates a

low resistance and good reversibility. Galvanostatic charge/discharge (GCD) curves of the EG@RuO$_x$ at different current densities show nearly symmetric triangular-shaped curves with clear redox signatures at around 0.3 V (Figure 3e), revealing good electrochemical reversibility and high coulombic efficiency, which is in good agreement with the CV curves. The rate performance confirms that the EG@RuO$_x$ shows superior rate performance and achieves the highest capacitance of 265 F g^{-1} at a current density of 1 A g^{-1} (Figure S11, Supporting Information). Even at very high current density of 30 A g^{-1}, the capacitance of the EG@RuO$_x$ reaches 180 F g^{-1}. This outstanding electrochemical performance of EG@RuO$_x$ could be explained by the alternating layered structure of EG and RuO$_x$ formed by the in situ growth method. The intercalated RuO$_x$ will increase the layer spacing and facilitates ion transport between the composite paper electrodes. EG is interspersed in the composite paper electrode as a current collector to effectively promote the charge transfer of RuO$_x$ in the composite paper electrode, thus exhibits high conductivity and excellent electrochemical performance. To further show the merits of the composite films as an electrode material, the EIS of EG@RuO$_x$ is shown in Figure 3f. From the Nyquist plot, the composite paper electrode shows a large slope of close to 90° at low frequency, which indicates fast ion diffusion. At the high frequency, see Figure 3f inset, the EG@RuO$_x$ shows a smaller charge-transport semicircle, which suggests that the alternating structure of composite electrode can ensure fast charge transfer between electrodes and electrolyte.

Considering the excellent electrochemical performance and complementary operating potential, a flexible solid-state ASCs is assembled using Mo$_{1.33}$C@L-DEA as the negative electrode and EG@RuO$_x$ as the positive electrode, as schematically illustrated in Figure 4a. The charge balance between the two electrodes, which is needed for the optimized performance of the asymmetric device, is achieved by balancing the mass loading prior to assembly. Figure 4b displays the potential windows of the Mo$_{1.33}$C@L-DEA (−0.35–0.3 V) and EG@RuO$_x$ (0–1.0 V) paper electrodes at the scan rate of 50 mV s^{-1}, showing that a similar amount of charge is being stored on each electrode. Finally, an operating potential window of up to 1.35 V is achieved for the ASCs, which yields higher energy density than the respective symmetric devices. The electrochemical performance of the ASCs is investigated by CVs at various scan rates. As shown in Figure 4c, the ASCs devices can be operated at a high scan rate, which indicates that the electrodes have low resistance and fast charge-discharge properties. Additionally, the GCD curves of the ASCs at different current density are shown in Figure 4d. The nearly symmetric shapes of these curves indicate rapid ion and electron transfer kinetics, high equilibrium of redox processes, and high coulombic efficiencies of the devices. The capacitances of the ASCs with the different current density are plotted in Figure 4e. The capacitance of the device reaches 205 F g^{-1} at a current density of 0.5 A g^{-1} and maintains a capacitance of 110 F g^{-1} at a current density of 30 A g^{-1}. This high rate performance can be attributed not only to capacity matching but also to kinetic
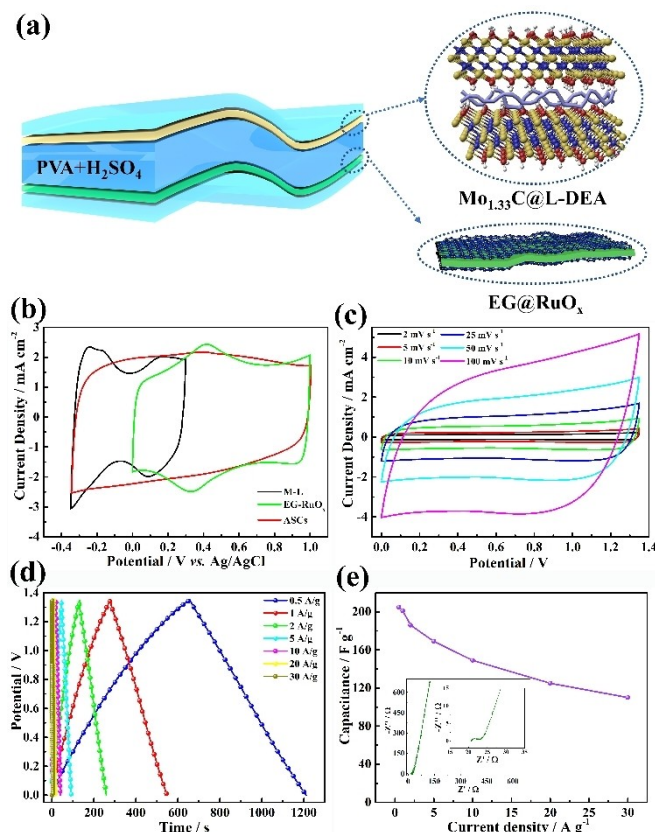
Figure 4. Electrochemical performance of the asymmetric supercapacitors. a) Schematic illustration of a solid-state asymmetric supercapacitor based on $Mo_{1.33}C@L\text{-}DEA$ and $EG@RuO_x$ as electrodes and PVA/H_2SO_4 as the electrolyte. b) Comparison of CV curves collected for $Mo_{1.33}C@L\text{-}DEA$ and $EG@RuO_x$ composite paper electrodes at scan rate of $100\ mV\,s^{-1}$. c) CV curves of corresponding ASCs devices at scan rates between 2 and $100\ mV\,s^{-1}$. d) Galvanostatic charge/discharge curves of ASCs at different current densities, e) Gravimetric rate performances of ASCs device. Inset: Electrochemical impedance spectroscopy (EIS) data of the ASCs devices.
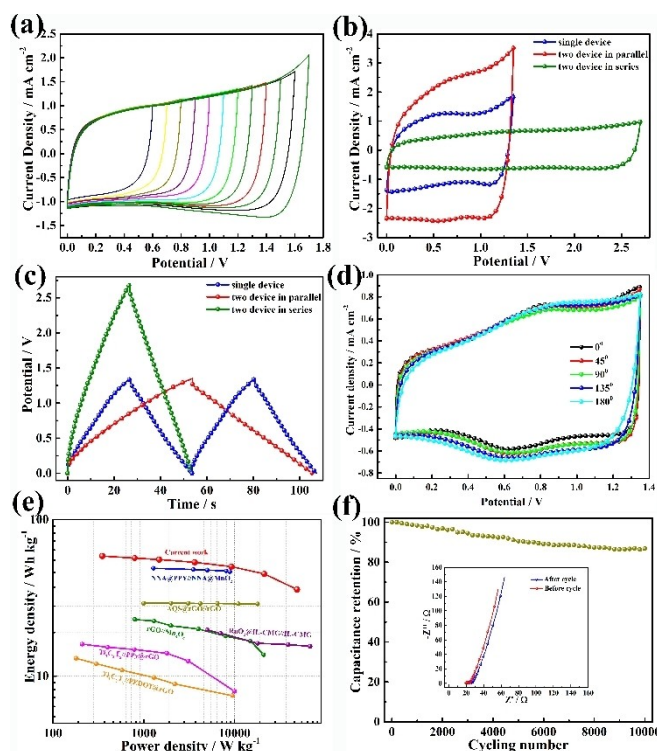

Figure 5. a) CV curves of the flexible ASCs device collected at different voltage windows. b) CV curves of ASCs devices connected in series and in parallel at a scan rate of $100\ mV\,s^{-1}$. A single device is shown for comparison. c) GCD curves of ASCs devices connected in series and in parallel at a current density of $1\ A\,g^{-1}$. d) CV curves of the ASCs device bended with different angles at $20\ mV\,s^{-1}$. e) Energy and power density of the ASCs device compared with previously reported device.[31–35] f) Cyclic stability of ASCs devices, inset: EIS data of the ASCs devices before and after cycle.

balance and fast redox kinetics of both electrodes. It can also be confirmed by the EIS spectrum (Figure 4e, inset).

Furthermore, the cell voltage of this ASCs device can be tuned from 0.5 to 1.7 V, as shown in Figure 5a. In order to explore the application prospect of ASCs, the devices are integrated by series and/or parallel connection to meet high voltage or capacitance requirements (Figure 5b and c). CV and GCD measurement show that an output voltage of 2.7 V can be obtained by two devices connected in series. Meanwhile, in the same voltage window of 1.35 V, the discharge time of ASCs connected in parallel is double that of a single one. These results indicate that the ASCs device has good reproducibility and can well manage practical power applications. The ASCs shows exceptional electrochemical stability under different bending angles. No significant deviation of the CV curves is observed when the bending angle changed from 0° to 180°, displaying excellent capacitance stability at different bending curvatures (Figure 5d). We have also plotted the Ragone plot shown in Figure 5e, comparing energy and power densities with previously reported supercapacitors. Our ASCs delivers an energy density of $51.9\ Wh\,kg^{-1}$ at power density of

$338.4\ W\,kg^{-1}$ and shows better performance than those of the reported electric double-layer capacitors or pseudocapacitors.[36–40] This high energy density is likely due to the dual fast pseudocapacitive behavior of the $Mo_{1.33}C$ MXene and the RuO_x. Long-term stability is a very important feature for commercially viable supercapacitors. Therefore, the cycling stability of the ASCs is evaluated by GCD tests at the current density of $5\ A\,g^{-1}$. The asymmetric device exhibits good cycling stability with capacitance retention of 87% and a coulombic efficiency of 100% over 10 000 cycles (Figure 5f). By comparison, the EIS of the ASCs demonstrates only a slight increase of the internal resistance at high frequency and the microstructure of the electrode materials has hardly changed after 10000 cycles (Figure 5f inset).

3. Conclusions

In summary, aligned layer structured MXene/biopolymer composite paper electrodes are obtained by self-assembly of negatively charged $Mo_{1.33}C$ MXene and amine-cations-functionalized lignin. The intercalation of L-DEA with the MXene layer leads to an increase in interlayer spacing and an improvement in charge transfer, which enables the composite electrode a maximum capacitance of $503.7\ F\,g^{-1}$. The $Mo_{1.33}C@L\text{-}DEA$

Batteries & Supercaps

Articles
doi.org/10.1002/batt.202000044

Chemistry Europe
European Chemical
Societies Publishing

composite structure also shows excellent stability and rate performance. Furthermore, the advantage of in situ grown RuO_x on EG is verified by enhanced capacitance, increased stability, smaller resistance, and rapid ion diffusion. The complementary potential windows of these two electrodes makes a perfect match for constructing an asymmetric device. The constructed ($Mo_{1.33}C@L$-DEA//EG@RuO_x) device operates at a voltage window of 1.35 V and delivers an energy density of 51.9 and 27.8 $Wh\,kg^{-1}$ at power densities of 338.4 and 40095 $W\,kg^{-1}$, respectively. Our work presents an effective strategy to design high-potential supercapacitors with increased energy density.

Experimental Section

Synthesis of the $Mo_{1.33}C$ MXene

$Mo_{1.33}C$ was synthesized as previously described.[12] Briefly, 1 g of $(Mo_{2/3}Sc_{1/3})_2AlC$ was added into 20 mL of 48% HF, stirring for 24 h at room temperature. After the reaction, the product was washed with deionized water. After washing, multilayer MXene was delaminated into single/few layer MXene by intercalating with TBAOH. 10 mL of 40% TBAOH water solution was added to the multilayer MXene, which was shaken manually for about 5 min. Extra TBAOH was removed by centrifuging at 5000 r.p.m for 5 min and followed by carefully rinsing with water for three times. Then, water was added to the intercalated powder and the mixture was shaken for 5 min, for delamination into single- or few layered MXene. Finally, homogeneous delaminated $Mo_{1.33}C$ MXene was obtained by centrifuging for 30 min at 3500 r.p.m.

Synthesis of L-DEA

1 g of alkali lignin was added into 20 ml of water, then NaOH solution (20%) was added to adjust the pH to 11. After stirring for 30 min at 80°C, 0.35 mg of diethanolamine was added. 0.27 g of formaldehyde solution (37%) was slowly added in half an hour, and then the mixture was stirred and refluxed for 3 h. The solution was then diluted with an appropriate amount of water, and 30% hydrochloric acid (HCl) solution was added to precipitate the lignin amine-based polyol. It was then allowed to stand still for 2–3 h, and was centrifuged to get the precipitated product. The precipitate was washed with dilute HCl (1 M), and then repeatedly washed with distilled water until pH was close to neutral. Finally, the precipitate was dried at 60°C for 10 h.

Synthesis of $Mo_{1.33}C@L$-DEA composite

The $Mo_{1.33}C@L$-DEA composites were prepared by mixing the L-DEA dispersion solution and the $Mo_{1.33}C$ colloidal solution. The mixture was stirred for 5 min and then vacuum-filtered onto nanoporous polypropylene membranes (Celgard 3501, 0.064 µm pore size, Celgard LLC) in air. Finally, the composites film was vacuum dried at 60°C for about 12 hours.

Graphite exfoliation

Graphite exfoliation was carried out in a two-electrode system, in which two graphite foils (Alfa Aesar) were used as cathode and anode, respectively. The electrodes were placed in parallel at a fixed distance of 1.0 cm. H_2SO_4 (0.1 M) was used as the electrolyte.

An alternating current (± 10 V, 0.1 Hz) was used to trigger the exfoliation process, in which anodic working bias switches every 5 seconds from positive ($+10$ V) to negative (-10 V), and vice versa. To avoid over-heat in the electrolyte, it was kept in ice bath during the entire exfoliation procedure. The suspended exfoliated graphene (EG) were collected with a PTFE membrane filter and wished with water by vacuum filtration. The graphene power was dispersed in DMF by sonication for 30 min. The un-exfoliated flakes and large particles were removed by centrifugation (3000 rpm, 10 min). The supernatant was used for further characterization and composite films fabrication.

Synthesis of EG@RuO_x composite

50 mg EG was dispersed in 25 ml H_2O by sonication for 30 min. Then, 50 mg $RuCl_3$ was added to the EG suspension and stirred for 30 min. After adjusting the pH to 7 by adding NaOH solution (1 M), the suspension was continuously stirred for 5 h at room temperature. A composite film was prepared by vacuum filtration with PTFE membrane filter (pore size 0.4 µm). The film was wished with ethanol and water for several times. Finally, the composites film was vacuum dried at 60°C for about 10 hours and then annealed at 300°C in air for 2 h.

Preparation of gel electrolyte

The polyvinyl alcohol (PVA)/H_2SO_4 gel electrolyte was prepared as follows: 1 g of PVA was added into 10 mL of deionized water and heated to 85°C while stirring until the solution became clear. Then, 1 g concentrated H_2SO_4 (98%) was added to the solution and stir from 15 min. The solution was used after cooling down to room temperature.

In the three-electrode configuration, the $Mo_{1.33}C$ or the composite film was used as working electrode, platinum foils as counter electrode and Ag/AgCl in 1 M KCl as the reference electrode using the aqueous solution containing H_2SO_4 (1 M) as the electrolyte. The all solid-state supercapacitors were fabricated using Au-coated polyethylene terephthalate substrate as the flexible conductive substrate and PVA/H_2SO_4 gel electrolyte as the solid electrolyte (≈ 45 µm). The mass loading of the $Mo_{1.33}C@L$-DEA is 1.24 $mg\,cm^{-2}$ and the EG@RuO_x is 1.92 $mg\,cm^{-2}$. First, the electrolyte was cast onto the electrodes, then was left in the fume hood at room temperature for 1 h to vaporize the excess water. Then the two pieces of electrodes were pressed together. The electrolyte was solidified and functioned as a glue holding all the device components together and improving the mechanical stability.

Characterizations

The electrochemical tests were performed using an Autolab PGSTAT 302 N (Metrohm AG, Netherlands) at room temperature. The impedance measurements were performed with a 5 mV amplitude in a frequency range from 10 mHz to 100 kHz. The morphology and microstructure of the different electrodes were investigated by means of field emission scanning electron microscopy (LEO 1550 Gemini) equipped with energy dispersive spectroscopy (EDS). XPS measurements were performed using monochromatic Al-Ka (1486.6 eV) radiation in a Kratos AXIS Ultra DLD system and a Scienta SES200 system. XRD was carried out on a PANalytical X'Pert diffractometer using Cu Kα radiation (45 KV and 40 mA). The zeta potential was measured by Malvern Zetasizer Nano ZS Analyzer. The samples were prepared by ultrasound to form a homogeneous dilute solution. Infrared spectra were

Batteries & Supercaps

Articles
doi.org/10.1002/batt.202000044

Chemistry Europe
European Chemical
Societies Publishing

recorded using a Bruker Vertex 70 Fourier transform infrared (FT-IR) spectrometer with samples in KBr pellets.

Conflict of Interest

The authors declare no conflict of interest.

[1] B. Conway, *Electrochemical Supercapacitors: Scientific Fundamentals and Technological Applications*, Kluwer Academic/Plenum, New York, **1999**.
[2] P. Simon, Y. Gogotsi, *Nat. Mater.* **2008**, *7*, 845–854.
[3] L. Yu, H. Hu, H. Wu, X. Lou, *Adv. Mater.* **2017**, 1604563.
[4] X. Zang, C. Shen, E. Kao, R. Warren, R. Zhang, K. S. Teh, J. Zhong, M. Wei, B. Li, Y. Chu, M. Sanghadasa, A. Schwartzberg, L. Lin, *Adv. Mater.* **2017**, 1704754.
[5] B. Mendoza-Sánchez, Y. Gogotsi, *Adv. Mater.* **2016**, *28*, 6104–6135.
[6] K. Qin, J. Kang, J. Li, C. Shi, Y. Li, Z. Qiao, N. Zhao, *ACS Nano* **2015**, *9*, 481–487.
[7] M. Naguib, M. Kurtoglu, V. Presser, J. Lu, J. Niu, M. Heon, L. Hultman, Y. Gogotsi, M. W. Barsoum, *Adv. Mater.* **2011**, *23*, 4248–4253.
[8] M. Naguib, O. Mashtalir, J. Carle, V. Presser, J. Lu, L. Hultman, Y. Gogotsi, M. W. Barsoum, *ACS Nano* **2012**, *6*, 1322–1331.
[9] M. Naguib, J. Halim, J. Lu, K. M. Cook, L. Hultman, Y. Gogotsi, M. W. Barsoum, *J. Am. Chem. Soc.* **2013**, *135*, 15966–15969.
[10] M. W. Barsoum, *MAX Phases: Properties of Machinable Ternary Carbides and Nitrides*, John Wiley & Sons, **2013**.
[11] M. Dahlqvist, J. Lu, R. Meshkian, Q. Tao, L. Hultman, J. Rosen, *Sci. Adv.* **2017**, *3*, e1700642.
[12] Q. Tao, M. Dahlqvist, J. Lu, S. Kota, R. Meshkian, J. Halim, J. Palisaitis, L. Hultman, M. W. Barsoum, P. O. Å. Persson, J. Rosen, *Nat. Commun.* **2017**, *8*, 14949.
[13] L. Qin, Q. Tao, A. E. Ghazaly, J. Fernandez-Rodriguez, P. O. Å. Persson, J. Rosen, F. Zhang, *Adv. Funct. Mater.* **2018**, *28*, 1703808.
[14] L. Qin, Q. Tao, X. Liu, M. Fahlman, J. Halim, P. O. Å. Persson, J. Rosen, F. Zhang, *Nano Energy* **2019**, *60*, 734–742.
[15] D. D. L. Chung, *J. Mater. Sci.* **2002**, *37*, 1475–1489.
[16] R. L. Ledoux, J. L. White, *J. Colloid Interface Sci.* **1966**, *21*, 127–260.
[17] M–Q. Zhao, C. Ren, Z. Ling, M. R. Lukatskaya, C. Zhang, K. L. V. Aken, M. W. Barsoum, Y. Gogotsi, *Adv. Mater.* **2015**, *27*, 339–345.
[18] M. Ghidiu, M. R. Lukatskaya, M–Q. Zhao, Y. Gogotsi, M. W. Barsoum, *Nature* **2014**, *516*, 78–81.
[19] M. R. Lukatskaya, O. Mashtalir, C. E. Ren, Y. Dall'Agnese, P. Rozier, P. L. Taberna, M. Naguib, P. Simon, M. W. Barsoum, Y. Gogotsi, *Science* **2013**, *341*, 1502–1505.
[20] H. Huang, H. Su, H. Zhang, L. Xu, X. Chu, C. Hu, H. Liu, N. Chen, F. Liu, W. Deng, B. Gu, H. Zhang, W. Qing, *Adv. Electron. Mater.* **2018**, 1800179.
[21] H. Huang, X. Chu, H. Su, H. Zhang, Y. Xie, W. Deng, N. Chen, F. Liu, H. Zhang, B. Gu, W. Deng, W. Yang, *J. Power Sources* **2019**, *415*, 1–7.
[22] H. Huang, J. He, Z. Wang, H. Zhang, L. Jin, N. Chen, Y. Xie, X. Chu, B. Gu, W. Deng, W. Yang, *Nano Energy* **2020**, *69*, 104431.
[23] Z. Ling, C. Ren, M–Q Zhao, J. Yang, J. M. Giammarco, J. Qiu, M. W. Barsoum, Y. Gogotsi, *Proc. Natl. Acad. Sci. USA* **2014**, *111*, 16676–16681.
[24] M. Boota, B. Anasori, C. Voigt, M–Q. Zhao, M. W. Barsoum, Y. Gogotsi, *Adv. Mater.* **2016**, *28*, 1517–1522.
[25] M. Zhu, Y. Huang, Q. Deng, J. Zhou, Z. Pei, Q. Xue, Y. Huang, Z. Wang, H. Li, Q. Huang, C. Zhi, *Adv. Energy Mater.* **2016**, *6*, 1600969.
[26] C. Chi, M. Boota, X. Xie, M. Zhao, B. Anasori, C. Ren, L. Miao, J. Jiang, Y. Gogotsi, *J. Mater. Chem. A* **2017**, *5*, 5260–5265.
[27] G. Milczarek, *Electroanalysis* **2007**, *19*, 1411–1414.
[28] G. Milczarek, O. Inganäs, *Science* **2012**, *335*, 1468–1471.
[29] G. Milczarek, M. Nowicki, *Mater. Res. Bull.* **2013**, *48*, 4032–4038.
[30] S. K. Kim, Y. K. Kim, H. Lee, S. B. Lee, H. S. Park, *ChemSusChem* **2014**, *7*, 1094–1101.
[31] A. M. Navarro-Suarez, N. Casado, J. Carretero-Gonzalez, D. Mecerreyes, T. Rojo, *J. Mater. Chem. A* **2017**, *5*, 7137–7145.
[32] F. N. Ajjan, N. Casado, T. Rebis, A. Elfwing, N. Solin, D. Mecerreyes, O. Inganäs, *J. Mater. Chem. A* **2016**, *4*, 1838–1847.
[33] K. Qin, E. Liu, J. Li, J. Kang, C. Shi, C. He, F. He, N. Zhao, *Adv. Energy Mater.* **2016**, *6*, 1600755.
[34] J. Yan, Z. Fan, W. Sun, G. Ning, T. Wei, Q. Zhang, R. Zhang, L. Zhi, F. Wei, *Adv. Funct. Mater.* **2012**, *22*, 2632 .
[35] F. N. Ajjan, M. J. Jafari, T. Rebis, T. Ederth, O. Inganäs, *J. Mater. Chem. A* **2015**, *3*, 12927–12937.
[36] C. Xu, Z. Li, C. Yang, P. Zou, B. Xie, Z. Lin, Z. Zhang, B. Li, F. Kang, C–P. Wong, *Adv. Mater.* **2016**, *28*, 4105–4110.
[37] M. Boota, Y. Gogotsi, *Adv. Energy Mater.* **2019**, *9*, 1802917.
[38] X. Wang, F. Wan, L. Zhang, Z. Zhao, Z. Niu, J. Chen, *Adv. Funct. Mater.* **2018**, 1707247.
[39] R. Shi, C. Han, H. Duan, L. Xu, D. Zhou H. Li, J. Li, F. Kang, B. Li, G. Wang, *Adv. Energy Mater.* **2018**, 1802088.
[40] B. G. Choi, S–J. Chang, H–W. Kang, C. P. Park, H. J. Kim, W. H. Hong, S. G. Lee, Y. S. Huh, *Nanoscale* **2012**, *4*, 4983–4988.